

Dynamical diffraction of x rays at grazing angle

Terrence Jach and P. L. Cowan

National Institute of Standards and Technology, Gaithersburg, Maryland 20899

Qun Shen and M. J. Bedzyk

Cornell High Energy Synchrotron Source, Wilson Laboratory, Cornell University, Ithaca, New York 14853

(Received 11 May 1988; revised manuscript received 5 October 1988)

We present details of the theory and experimental observation of dynamical diffraction of x rays at grazing angle from crystal planes normal to a surface. We are able to associate different features of the specularly reflected and diffracted-reflected beam fluxes with the contributions from the α and β branches of the dispersion surfaces. The theory predicts surface propagation modes to which internal and external beams can couple only through the diffraction process. An experiment is described in which the specularly reflected and reflected-diffracted beams were simultaneously observed for 8-keV x rays incident on germanium. The agreement with first-order theory is good, but we observe systematic deviations. We present calculations that illustrate how eigenstates of the wave fields, which are x-ray standing waves with nodal planes normal to the surface of the crystal, can be used to obtain atomic registration at a surface or interface.

I. INTRODUCTION

Waves can penetrate into regions where their propagation is nominally forbidden, as has been demonstrated by phenomena ranging from frustrated total internal reflection¹ to particle tunneling. In the conventional plane-wave representation² these effects are described by evanescent waves, i.e., waves whose wave vector consists of real and imaginary components. When the index of refraction of materials is generally less than unity, such as at x-ray energies, the phenomenon is manifested as total external reflection, with wave solutions decaying exponentially into the surface of the medium. The short decay length of evanescent x rays makes them attractive as a surface probe.

It has been natural to combine the surface enhancement of grazing-incidence x rays with diffraction to obtain the ordering of surface layers.³ The geometry of surface diffraction at grazing angle is the third of the three limiting geometries of x-ray diffraction (the symmetric Bragg and Laue cases being the other two), which are determined by symmetric orientation of the surface relative to the crystal planes and the dispersion plane. It differs from the other two geometries in that total external reflection is significant over much of the phase space of the diffraction problem, including away from the Bragg condition.

There has recently been a great deal of interest in effects predicted by the dynamical theory of x-ray diffraction in crystals in the grazing-angle geometry.⁴⁻¹⁰ Synchrotron radiation of sufficient intensity and angular collimation has allowed the resolution of these effects for the first time.¹⁰ Furthermore, the effects predicted by the dynamical theory of grazing-angle x rays near a diffraction condition have potential application to the study of interfaces as well as surfaces.

The purpose of this paper is severalfold. (1) We rederive the two-beam approximation to the dynamical theory of x-ray diffraction in the grazing-angle geometry. This derivation, in terms of angles, permits a useful discussion of the interaction between the different x-ray beams at the surface and makes it easier to relate the data to the dispersion surface in this geometry. (2) We describe the details of an experimental configuration used to obtain diffraction and reflection of synchrotron radiation at grazing angles. (3) We present new results obtained from the diffraction of x rays of 8 keV energy from germanium. The results cover a much wider region of the phase space in the vicinity of the diffraction condition than previously reported¹⁰ and are calibrated for the first time in normalized flux. These results are generally in good agreement with the predictions of the theory, but show deviations from the lowest-order approximations in the two-beam theory. (4) In the last part of this paper we shall discuss the production of x-ray standing waves in this geometry. X-ray standing waves (XSW's) generated in the Bragg geometry¹¹ have proven to be a major new tool for the study of atoms at or near surfaces,^{12,13} and the grazing-angle geometry offers the possibility of generating these waves with a wave vector parallel to a surface or an interface.

II. THEORY

In this section we review a coherent theoretical treatment of all the beams present in the grazing-angle geometry, using the two-beam approximation to the dynamical theory. We demonstrate the general manner in which dispersion surface solutions of the diffraction treatment couple to the incident and exiting beams. We shall show that under certain circumstances special surface waves exist whose decay rates into the bulk or the

vacuum are controllable.

The original derivation of the diffraction intensity was done by Afanas'ev and Melkonyan.⁴ Various aspects of the problem have been treated by Aleksandrov *et al.*,⁵ and early theory and experiments have been summarized in a review by Andreev.⁶ The complete solution which included the intensities of the specularly reflected beams was presented by Cowan⁷ and Andreeva and Borisova.⁸ Cowan produced results for standing-wave fields.

We would like to derive the angles and fluxes of the various x-ray beams associated with the surface dynamical diffraction problem in a slightly different way here. The notation used follows the treatment of dynamical diffraction by Batterman and Cole (hereafter BC).¹⁴

We shall consider grazing-angle diffraction (GAD) in the fully symmetric case where the surface is a particular crystal plane, and the diffraction is due to another set of planes which are normal to the surface. That is, the scattering is done by a reciprocal-lattice vector which is parallel to the surface. We shall derive results for an x-ray beam with σ polarization. We restrict ourselves to a range of angles where the two-beam approximation is valid.

Figure 1 shows the geometry and includes the beams which can result from coupling to solutions inside and outside the crystal for an x-ray beam with wave vector \mathbf{k}_0 incident on the surface at an angle φ . Since translational symmetry is preserved parallel to the surface but not normal to it, only momentum parallel to the surface is conserved,

$$\mathbf{k}_{0\parallel} = \mathbf{k}_{s\parallel} = \mathbf{K}_{0\parallel}, \quad (1)$$

where \mathbf{k}_s is the wave vector of the specularly reflected beam outside the crystal, and \mathbf{K}_0 is the wave vector of the undiffracted beam propagating inside the crystal. Outside the crystal,

$$|\mathbf{k}_0| = |\mathbf{k}_s| = |\mathbf{k}_H|, \quad (2a)$$

so

$$\varphi_s = \varphi. \quad (2b)$$

The parallel component of the diffracted beam is determined simply by adding the reciprocal-lattice vector \mathbf{H}

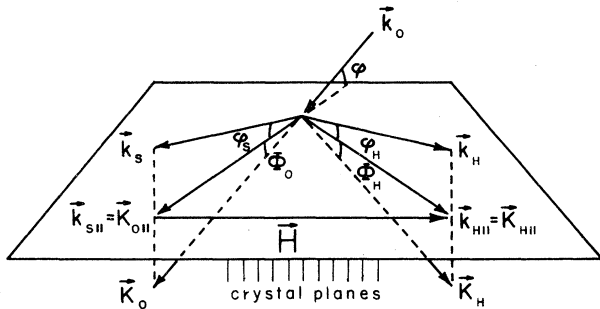


FIG. 1. Diagram showing beams which can result from an x-ray beam of wave vector \mathbf{k}_0 incident on a crystal and diffracted by a reciprocal-lattice vector \mathbf{H} parallel to the crystal surface.

associated with the diffracting planes to the parallel component of the incident beam $\mathbf{k}_{0\parallel}$, where we express the geometrical Bragg condition

$$\left| \frac{\mathbf{H}}{2} \right| = |\mathbf{k}_0| \sin \theta_B. \quad (3)$$

The components of the wave vectors projected on the surface of the crystal are not affected by the index of refraction inside the crystal and are shown in Fig. 2. The angle of the diffracted beam with respect to the diffracting planes does not have to be the same as the angle θ of the incident beam to those planes.

We get

$$k_{0\parallel}^2 - k_{0\parallel}^2 \sin^2 \theta = k_{H\parallel}^2 - (H - k_{0\parallel} \sin \theta)^2. \quad (4)$$

By using $\Delta \theta = \theta - \theta_B$,

$$\cos^2 \varphi - \sin^2 (\Delta \theta + \theta_B) = \cos^2 \varphi_H - [2 \sin \theta_B - \sin (\Delta \theta + \theta_B)]^2. \quad (5)$$

For small angles φ , the result is

$$\varphi_H^2 = \varphi^2 + 2 \Delta \theta \sin 2 \theta_B. \quad (6)$$

We now consider the solutions inside the crystal. Following BC we consider that the wave vectors inside the crystal are complex, with the imaginary part normal to the surface. The periodic dielectric constant of the crystal is expanded into Fourier components of the reciprocal lattice,

$$\epsilon(\mathbf{r}) = 1 - \Gamma \sum_H F_H e^{-2\pi i \mathbf{H} \cdot \mathbf{r}}, \quad (7)$$

where

$$\Gamma = \frac{r_e \lambda^2}{\pi V},$$

and r_e is the classical electron radius, λ is the x-ray wavelength, and V is the volume of the unit cell. The magnitudes of the wave vectors in the incident and diffracted direction are given by¹⁴

$$K_0^2 = k_0^2 (1 - \Gamma F_0) + 2k_0 \xi_0 \quad (8)$$

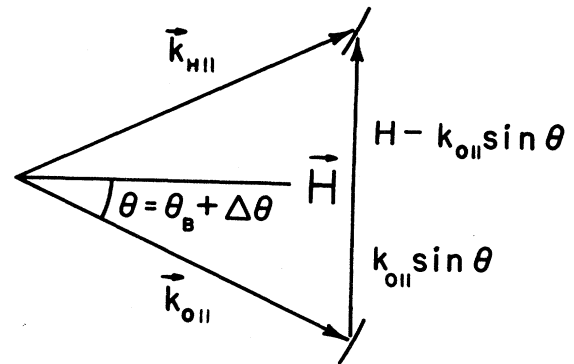


FIG. 2. Components of the wave vector parallel to the crystal surface which are conserved.

and

$$K_H^2 = k_0^2(1 - \Gamma F_0) + 2k_0\xi_H, \quad (9)$$

where $1 - \Gamma F_0$ is the average dielectric constant for the crystal, and

$$\xi_0\xi_H = \frac{k_0^2\Gamma^2F_HF_{\bar{H}}}{4} \quad (10)$$

is determined by the secular equation solving Maxwell's equations inside the periodic medium.

As is well known in the conventional dynamical theory of diffraction, the solutions of the secular equation correspond to linear combinations of diffracted and undiffracted beams propagating inside the crystal, resulting in a Bloch wave modulated with the periodicity of the lattice which is diffracting. Equation (10) is the fundamental equation describing the loci of such solutions in reciprocal space, known as dispersion surfaces. The quantities ξ_0, ξ_H are the fractional difference in magnitude of the actual refracted wave vectors from the mean value they would have for an isotropic dielectric constant ($1 - \Gamma F_0$). The solutions as they would look for $K_{01} = K_{H1} = 0$ are shown in Fig. 3. The loci of solutions known as the α and β branches correspond to standing waves with nodes on the diffraction planes and between the diffraction planes, respectively. From BC we readily determine that for the grazing-angle geometry these quantities are given by

$$\xi_{0i} = \frac{k_0(\Gamma F_H \Gamma F_{\bar{H}})^{1/2}}{2} [\eta \pm (\eta^2 + 1)^{1/2}] \quad (11a)$$

and

$$\xi_{Hi} = \frac{k_0(\Gamma F_H \Gamma F_{\bar{H}})^{1/2}}{2[\eta \pm (\eta^2 + 1)^{1/2}]}, \quad (11b)$$

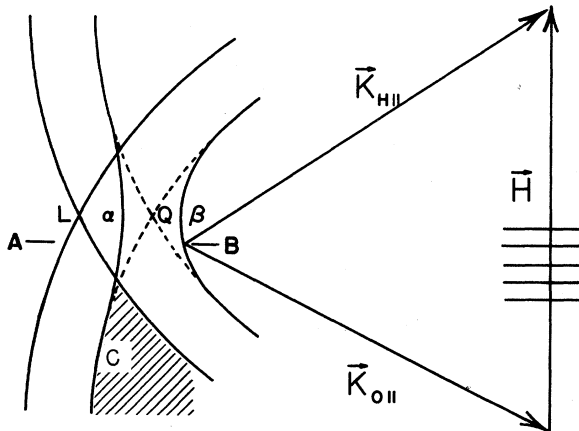


FIG. 3. Dispersion surfaces occurring at the diffraction condition. The loci of all possible incident and diffracted wave vectors in the vacuum intersect at L . The loci of those wave vectors in the crystal would intersect at Q if the periodic components of the dielectric constant were not present. The orientation of the crystal planes is shown. The hatched region C designates where diffracted beams exist but are evanescent into the vacuum.

where the $+$ sign is taken for $i = \alpha$, the $-$ sign for $i = \beta$, and

$$\eta = (\Gamma F_H \Gamma F_{\bar{H}})^{-1/2} \Delta \theta \sin 2\theta_B. \quad (12)$$

We make the approximation

$$K_{0i} = k_0(1 - \frac{1}{2}\Gamma F_0 + \xi_{0i}/k_0) \quad (13a)$$

and

$$K_{Hi} = k_0(1 - \frac{1}{2}\Gamma F_0 + \xi_{Hi}/k_0), \quad (13b)$$

where $i = \alpha, \beta$. Then the phase-matching conditions (1) at the crystal boundary take the forms

$$k_0 \cos \varphi = K_{0i} \cos \Phi_{0i} \quad (14a)$$

and

$$k_H \cos \varphi_H = K_{Hi} \cos \Phi_{Hi}, \quad (14b)$$

where Φ_{0i} and Φ_{Hi} are the angles that the internal beams K_{0i} and K_{Hi} make with the surface. We shall be concerned only with the case where φ and Φ_{0i} are small, so we keep only the leading terms in the series to get

$$\Phi_{0i}^2 = \varphi^2 + 2\xi_{0i}/k_0 - \Gamma F_0. \quad (15a)$$

When we refer to the critical angle φ_c , we shall be ignoring the diffractive component, i.e., $0 = \varphi_c^2 - \Gamma F_0$. By a similar process,

$$\Phi_{Hi}^2 = \varphi_H^2 + 2\xi_{Hi}/k_0 - \Gamma F_0, \quad (15b)$$

where φ_H is obtained from (6).

The circumstances under which the internal solutions inside the crystal are coupled to external solutions is readily visualized. In the geometry of surface diffraction at glancing incidence, the crystal planes shown in Fig. 3 are normal to the surface, and the wave vectors \mathbf{K}_0 and \mathbf{K}_H are nearly parallel to it. The reciprocal-lattice vector \mathbf{H} lies along the surface of the crystal, and the intersecting segments of circles of constant wave vector are really the intersections of spheres of constant wave vector, when we take into account the possibility that the incident and propagating beams are not strictly parallel to the crystal surface. Figure 4 shows the surfaces traced out by all possible angles of incidence and exit from the surface diffraction problem. The standard Ewald triangle shown in Fig. 3 is the intersection of these spheres with the surface of the crystal. A vertical slice through the section AB is illustrated in Fig. 5. Because translational symmetry is broken in passing through the surface, it is permitted to add an arbitrary component normal to the surface to a wave vector on one side of the interface to allow coupling to a wave vector on the other side. Figure 5 shows a vertical cross section through the dispersion surfaces illustrating this coupling for three different angles of incidence.

For $\varphi = \varphi_3$, the angle of incidence is sufficiently large that a surface normal couples the incident beam not only to a specularly reflected and a reflected-diffracted beam, but to tie points for an α -branch and a β -branch solution propagating in the crystal as well. Other tie points occur

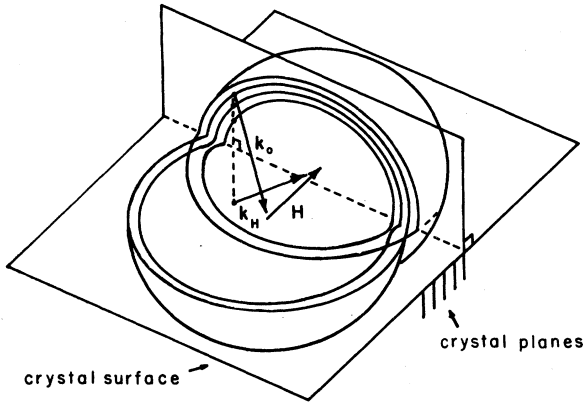


FIG. 4. Generalization of the dispersion surface of Fig. 3 to three dimensions in the GAD geometry. A surface normal is shown (dashed line) along which arbitrary wave vectors may be added to permit coupling of wave vectors into and out of the crystal. The cross section is displaced from the symmetry line of Fig. 3.

where the surface normal cuts through dispersion surfaces, but these are not depicted because they correspond to sources originating inside the crystal which are unphysical.

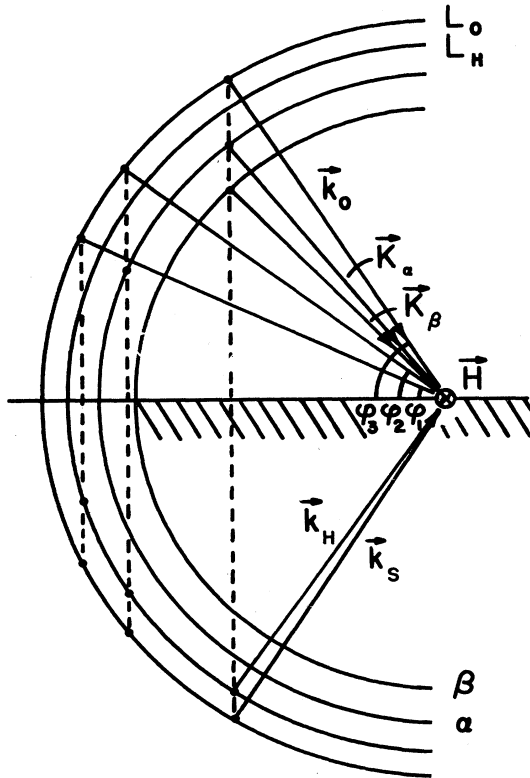


FIG. 5. Expanded view of the cross section of the dispersion surfaces shown in Fig. 4, normal to the surface of the crystal (hatched). The cut is taken through AB of Fig. 3. The tie points are illustrated for internal and external wave vectors at three different angles of incidence φ .

For a lower angle of incidence, $\varphi = \varphi_2$, we see that a surface normal can no longer couple the incident beam to a tie point on the β branch, but does couple to all the other solutions. In principle, this angle will result in a stronger specular reflection and reflected-diffracted beam.

For a very low angle of incidence, $\varphi = \varphi_1$, we see that the surface normal is no longer capable of coupling the incident beam to any solution which propagates inside the crystal, but surprisingly is able to couple to an external reflected-diffracted beam as well as to a specular reflection. In the vicinity of a diffraction condition, there is not a single critical angle for total external reflection, but two. Internal solutions with real wave vectors do not couple to the incident beam at very low angles because it is impossible to obtain a phase match at the boundary. If we consider internal solutions which are complex, however, it is possible to couple such wave vectors to the incident beam. Thus there can be evanescent solutions which decay exponentially into the crystal. These solutions also give rise to a reflected-diffracted beam and will be discussed later. From (6) and (15a) and (15b), they occur under conditions where

$$\varphi^2 < \Gamma F_0 - 2\xi_{0i}/k_0. \quad (16)$$

The penetration depths are determined from the imaginary components

$$K_{0i\perp} = K_{Hi\perp} = K_0 \sin \Phi_{0i} \approx k_0 \Phi_{0i}. \quad (17)$$

There is one more case in which the diffracted solution can become evanescent. From Eq. (6) it is seen that for

$$\varphi^2 < -2\Delta\theta \sin \theta_B \quad (18)$$

φ_H becomes imaginary. The normal component of the reflected-diffracted beam,

$$k_{H\perp} \approx k_0 \varphi_H, \quad (19)$$

is also imaginary. Under these conditions, the reflected-diffracted beam is evanescent *into the vacuum*. One way of understanding this result can be seen in Fig. 3. In the GAD geometry it is possible to have an α -branch solution in which the wave vector created by diffraction is longer than the vacuum wave vector,⁶ the hatched region of the α branch labeled C in Fig. 3. While this solution does not escape as a propagating beam, it is observed indirectly.¹⁰ A diffracted beam can be created which is evanescent both into the crystal and into the vacuum, analogous to a surface plasmon. Such a beam has a wave vector which is real only along the surface of the crystal.

We now proceed to calculate the amplitudes of the electric fields involved in the problem. For σ polarization the requirement at the boundary of the crystal are that the fields E_{\parallel} and D_{\perp} be continuous. The total electric field in the crystal is given by

$$\mathbf{E} = \mathbf{E}_{0i} e^{-2\pi i \mathbf{K}_0 \cdot \mathbf{r}} + \mathbf{E}_{Hi} e^{-2\pi i \mathbf{K}_H \cdot \mathbf{r}}, \quad (20a)$$

and outside the crystal by

$$\mathbf{E} = \mathbf{E}_0 e^{-2\pi i \mathbf{k}_0 \cdot \mathbf{r}} + \mathbf{E}_s e^{-2\pi i \mathbf{k}_s \cdot \mathbf{r}} + \mathbf{E}_H e^{-2\pi i \mathbf{k}_H \cdot \mathbf{r}}. \quad (20b)$$

The boundary conditions translate into the following expressions for the field amplitudes at the surface:

$$E_0 + E_s = E_{0\alpha} + E_{0\beta}, \quad (21a)$$

$$E_H = E_{H\alpha} + E_{H\beta} \quad (21b)$$

and

$$\varphi(E_0 - E_s) = \Phi_{0\alpha}E_{0\alpha} + \Phi_{0\beta}E_{0\beta}, \quad (22a)$$

$$-\varphi_H E_H = \Phi_{H\alpha}E_{H\alpha} + \Phi_{H\beta}E_{H\beta}, \quad (22b)$$

where we assume that φ , Φ_{0i} , and Φ_{Hi} are small.

From (21b) and (22b) one immediately obtains

$$E_{H\alpha} = E_H \left[\frac{\Phi_{H\beta} + \varphi_H}{\Phi_{H\beta} - \Phi_{H\alpha}} \right], \quad (23a)$$

$$E_{H\beta} = -E_H \left[\frac{\Phi_{H\alpha} + \varphi_H}{\Phi_{H\beta} - \Phi_{H\alpha}} \right] \quad (23b)$$

and

$$2\varphi E_0 = (\varphi + \Phi_{0\alpha})E_{0\alpha} + (\varphi + \Phi_{0\beta})E_{0\beta}. \quad (24)$$

The relationship between E_{Hi} and E_{0i} inside the crystal at a tie point on one of the dispersion surfaces is obtained from BC,

$$E_{Hi} = -\frac{2\xi_{0i}}{k_0 \Gamma F_H} E_{0i} = w_i E_{0i}, \quad i = \alpha, \beta. \quad (25)$$

Combining (23a), (23b), (24), and (25), we determine that

$$E_H = \frac{2E_0\varphi(\Phi_{H\alpha} - \Phi_{H\beta})w_\alpha w_\beta}{w_\alpha(\varphi + \Phi_{0\beta})(\Phi_{H\alpha} + \varphi_H) - w_\beta(\varphi + \Phi_{0\alpha})(\Phi_{H\beta} + \varphi_H)} \quad (26)$$

and

$$E_s = E_0 \left[\frac{w_\alpha(\varphi - \Phi_{0\beta})(\Phi_{H\alpha} + \varphi_H) - w_\beta(\varphi - \Phi_{0\alpha})(\Phi_{H\beta} + \varphi_H)}{w_\alpha(\varphi + \Phi_{0\beta})(\Phi_{H\alpha} + \varphi_H) - w_\beta(\varphi + \Phi_{0\alpha})(\Phi_{H\beta} + \varphi_H)} \right]. \quad (27)$$

In addition to the electric fields of the beams which are capable of escaping the crystal, it will be useful to calculate the x-ray standing-wave fields at the surface, which are capable of exciting atoms in the crystal near the surface or atoms of an adsorbate on the surface. It is possible to have a large modulation at the surface, even in the case where the diffracted beam cannot leave the crystal.

III. THE EXPERIMENT

The experimental configuration for GAD is shown in Fig. 6. The experiment whose results are presented here was performed on a bending-magnet beamline at the Cornell High Energy Synchrotron Source (CHESS).

X rays from the synchrotron were diffracted through a double-crystal monochromator, tuned to 7.9 keV. The vertically reflecting monochromator was implemented with a symmetrically cut Si(220) first crystal and an asymmetrically cut Si(220) second crystal. The magnification factor of the second crystal was greater than 50 at the energy 7.9 keV. The combination provided high collection efficiency, angular collimation in the vertical dimension, and angular displacement of harmonic radiation. The beam was then defined by slits to a horizontal width of about 0.1 mm. After passing through an ion chamber used to normalize the intensity, the beam was incident on the sample crystal. This consisted of a germanium crystal with a (111) surface polished to an optical finish, positioned so that its surface normal was nearly perpendicular to the incident beam. The sample was mounted on a two-circle goniometer so that the angle of incidence φ and the rotation about the surface normal θ could be varied independently.

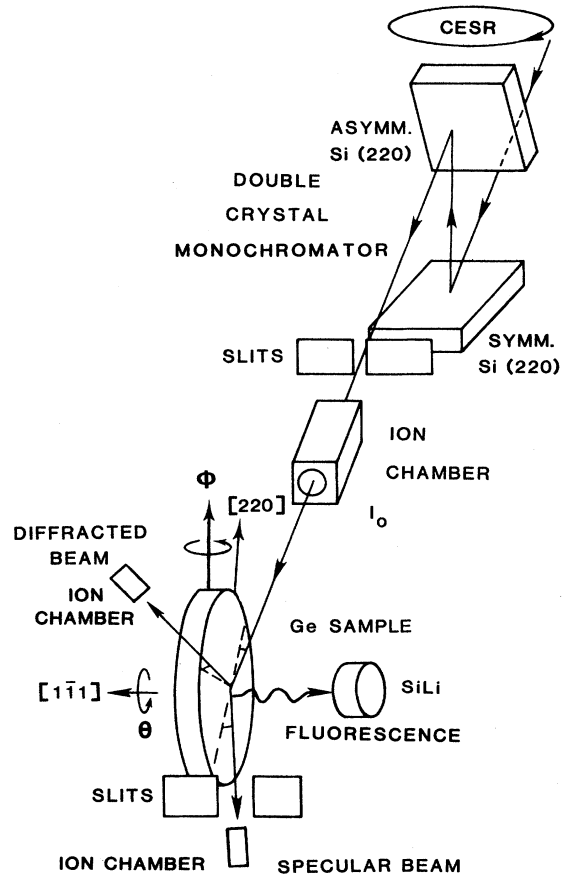


FIG. 6. Schematic diagram of the experiment.

The incident energy was such that for the (220) reflection of germanium $\theta_B = 23.1^\circ$. The combination of vertical slits and the synchrotron-source diameter limited the horizontal divergence of the beam to $250 \mu\text{rad}$ (compared to a critical angle for Ge of 4.5 mrad). The asymmetrically cut second monochromator crystal limited the vertical divergence of the beam to $1.4 \mu\text{rad}$ (compared to the Bragg rocking-curve width of $22 \mu\text{rad}$ at this energy for Ge). In previous investigations of GAD,^{9,15} beam intensities and angular resolution have limited the resolution of dynamical effects in both φ and $\Delta\theta$. In addition, the high degree of collimation which we were able to employ provided an input beam which was a close approximation to the plane-wave source upon which the theory is based.

Because of the grazing-angle geometry of this experiment, the scattering which gives rise to diffraction is confined to a thin layer of atoms near the surface. It is much more important than in the Bragg geometry that the surface be defect and stress free. The crystal surface was polished using an etching polishing compound. Immediately before the experiment, the surface oxide was

removed with an HF etch and rinsed in an iodine-methanol solution to provide a passivating monolayer of iodine. The surface was maintained in helium at atmospheric pressure thereafter to minimize further chemical reaction.

The specular and diffracted beam fluxes were monitored with ion chambers using Ar gas. An additional slit was employed between the sample and the specular ion chamber to ensure that the component of the incident beam which might pass by the sample was not collected as specular beam. The actual photon-count rate observed under the conditions of specular reflection was typically $2 \times 10^7 \text{ s}^{-1}$ with a diffracted beam count of the same order.

IV. RESULTS

Figures 7(a) and 7(b) show two views of the normalized flux of the specularly reflected beam (i.e., reflectivity) calculated for 7.9-keV x rays incident on the Ge surface as a function of φ and $\Delta\theta$. It is convenient to visualize the plane of the φ and $\Delta\theta$ axes as identical to the surface de-

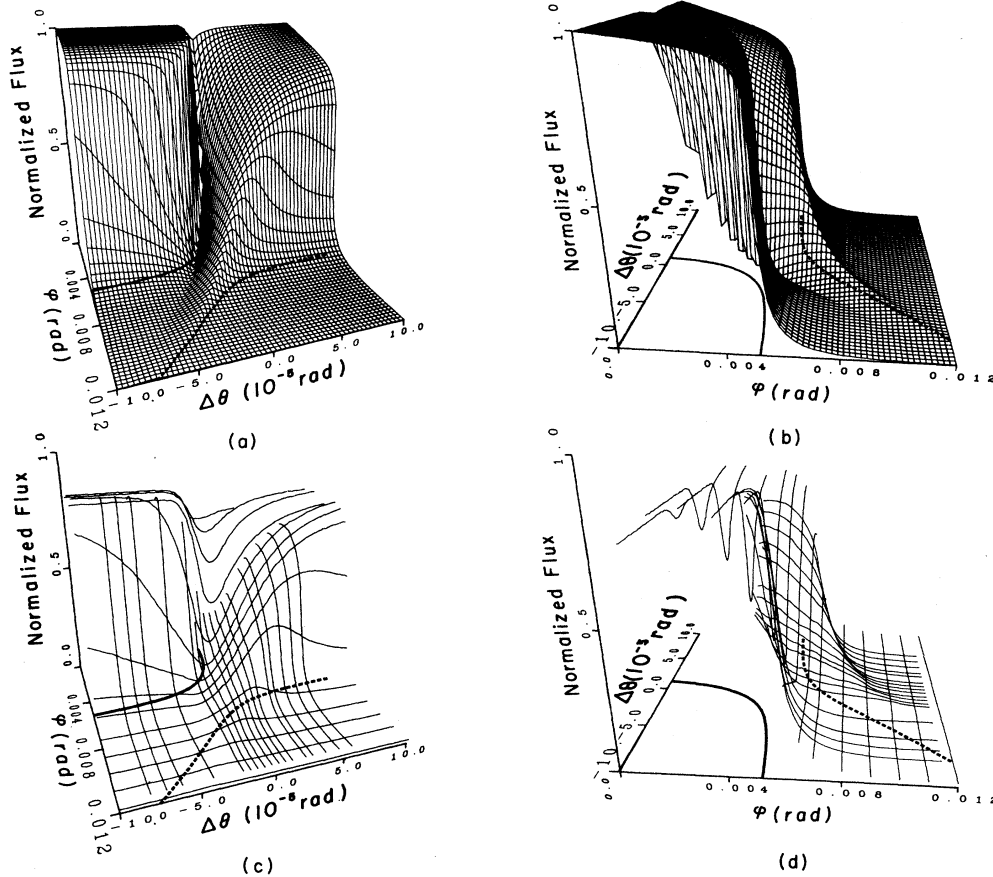


FIG. 7. Comparison of theoretical and experimental fluxes for the specular beam from the Ge(220) reflection at 7.9 keV, $\varphi_c = 5.4 \text{ mrad}$. The fluxes are normalized to the incident beam and plotted as a function of $\Delta\theta$ and φ . The calculated reflectivity plot is viewed from two different perspectives in (a) and (b), and corresponding experimental data are shown in (c) and (d). The positions of the α and β branches of the dispersion surfaces for $K_{01} = K_{H1} = 0$ are plotted, respectively, as solid and dashed lines in the φ - $\Delta\theta$ plane.

picted in Fig. 3, and rotated so that the vector $\mathbf{K}_{0\parallel}$ is parallel to the φ axis. Decreasing the angle φ corresponds to increasing $K_{0\parallel}$, and linear motion along the $\Delta\theta$ axis corresponds to small changes in the $\Delta\theta$ of the actual vector on the dispersion surface. Thus the α and β branches, when plotted in Fig. 7 as a function of φ and $\Delta\theta$, are geometrically almost identical to their actual shape on the Ewald plot in Fig. 3.

Data from the experimental measurement of the specularly reflected beam at 7.9 keV are plotted in Figs. 7(c) and 7(d). The data were obtained by holding φ constant and varying $-100 < \Delta\theta < 100$ μrad and by holding $\Delta\theta$ constant and varying $0 < \varphi < 12$ mrad. Data collected for $\varphi < 4$ mrad were corrected for an interception area of the sample less than the cross section of the incident beam and for obstruction of the reflected beam. All of the data were then normalized to the magnitude of the straight through beam in the specular beam ion chamber in order to give absolute reflectivities. When these corrections were made, the theoretical and experimental values for the specular reflectivity were in generally good agreement.

If $\varphi < \varphi_c$, as $\Delta\theta$ is varied, we observe a high reflectivity, except in the vicinity of the Bragg reflection,

where we observe a "canyon of diffraction" [Figs. 7(a) and 7(c)]. Inside this "canyon," as seen in Figs. 7(b) and 7(d), the reflectivity for $\Delta\theta = \text{const} \approx 0$ shows a two-step change with increasing φ . This corresponds to cutting across the thresholds for the α then the β branch. As shown in Figs. 7(b) and 7(d), the reflectivity in the vicinity of the Bragg condition $\Delta\theta \approx 0$ continues to be high for $\varphi > \varphi_c$ because the dielectric constant sampled by the β -branch solution is greater than the average, so the critical angle is also greater.

When plotted in this manner, the data demonstrate that reflectivity on one side of the "canyon of diffraction" is due to coupling to solutions in the α branch, and on the other side to coupling to the β branch. While it seems obvious that there should be a dip in the specular beam flux at the Bragg condition due to energy going into the diffracted beam, there is also a maximum in that flux above the critical angle.

Figures 8(a) and 8(b) show two views of a plot of the calculated reflected-diffracted beam flux under the same conditions as the specular beam in Fig. 7. The experimentally observed flux is shown in Figs. 8(c) and 8(d). The diffracted-beam data were corrected for $\varphi < 4$ mrad in the manner described above for the specular beam data

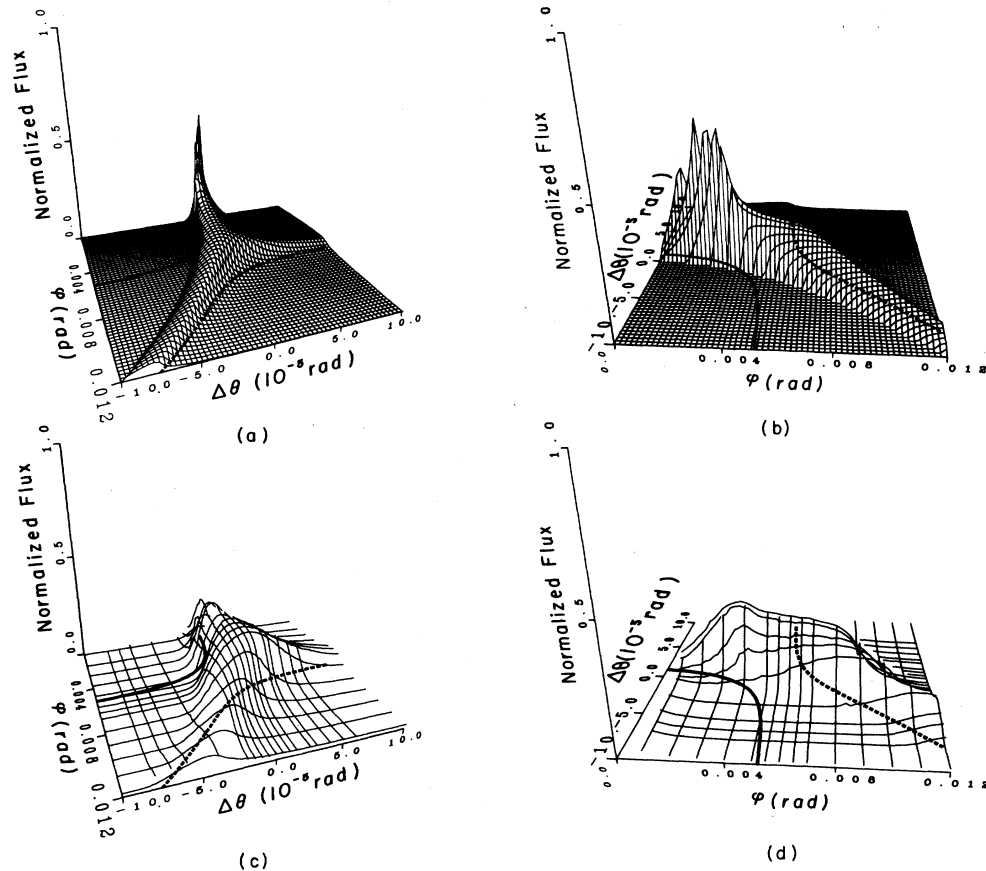


FIG. 8. Comparison of theoretical and experimental fluxes for the reflected-diffracted beam from the Ge(220) reflection at 7.9 keV, $\varphi_c = 5.4$ mrad. The fluxes are normalized to the incident beam and plotted as a function of $\Delta\theta$ and φ . The calculated flux is viewed from two different perspectives in (a) and (b), and corresponding experimental data are shown in (c) and (d). The positions of the α and β branches of the dispersion surfaces are plotted as described in Fig. 7.

and normalized to the incident flux. We present the data in comparison with an unbroadened calculation so that details predicted by the theory are shown in their true widths.

We note that shifts in the observed diffraction angle and width of the reflected-diffracted peak with angle of incidence are explained by the locations of the α and β branches of the dispersion surface. A sharp cusp in diffracted beam flux for $\varphi \approx 2$ mrad is seen to occur at the threshold for coupling to the α branch. We observe further that the reflected-diffracted beam coupled to the α branch is cut off for some value of $\Delta\theta < 0$, the region designated C in Fig. 3.

We have experimentally observed that the β -branch solution gives high reflectivity and diffracted-beam intensity for angles of incidence $\varphi > \varphi_c$, as predicted by the first-order theory. It is seen by comparing Figs. 8(a) and 8(c), however, that there is a systematic deviation occurring in the θ position of the observed diffracted beam with increasing angle of incidence, compared to the position predicted by the calculation. It is evident that higher-order corrections become significant at relatively small φ .

V. DISCUSSION

The GAD geometry offers the possibility of observing grazing-angle x-ray standing-wave (GAXSW) effects similar to those observed in the Bragg geometry.¹¹⁻¹³ In this geometry, however, the x-ray standing wave (i.e., the Bloch-wave modulation caused by the interference of the various beams above or below the surface) has nodal planes normal to the crystal surface. By changing φ or $\Delta\theta$ so as to vary the coupling of the incident wave between the α - and β -branch solutions, the phase of the x-ray standing wave may be continuously varied through an angle of π . The nodes of the standing wave are translated parallel to the surface by up to one-half the real-space distance determined by the reciprocal-lattice vector which is involved in the diffraction.

Figure 9 shows the x-ray intensity versus $\Delta\theta$ calculated from Eqs. (20b), (26) and (27) at four possible atomic positions on the Ge unit cell for $\varphi = 5.4$ mrad at 8 keV. The calculation is made for atoms at a height of 2.5 Å above the Ge (111) surface. The intensities, normalized to the incident electric field, correspond to an absorbate atom located along the reciprocal-lattice vector direction on the crystal surface for $r = 0, a/4, a/2$, and $3a/4$, where a is the distance between the diffracting planes. Near φ_c the scan in $\Delta\theta$ gives the maximum excursion in the surface standing-wave intensity, since it cuts directly across from an α -branch solution to a β -branch solution to the maximum extent. In practice, the yield of x-ray fluorescence radiation, photoelectrons, Auger electrons, etc. for atoms on or near the surface would be fitted by such a plot, according to their coherent position in the unit cell.

GAXSW effects obviously occur in the atoms of the substrate as well as in an overlayer. Large changes in the penetration depth of the x rays in the vicinity of the diffraction condition cause significant deviations from the amount of fluorescence due to a single layer of atoms at

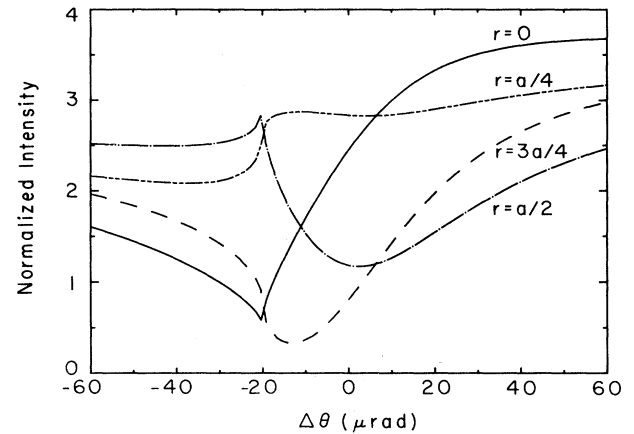


FIG. 9. Intensity of the electric field near the surface of a crystal vs $\Delta\theta$ for $\varphi = 5.4$ mrad. Curves are shown for atoms located on the diffraction planes ($r=0$) and at three interplanar sites along the \mathbf{H} direction. The intensity is calculated for a Ge(220) reflection at 8 keV and normalized to the incident beam.

the surface. Figure 10 is a plot of the fluorescence yield of 1.2-keV Ge $L\alpha$ radiation from a similar Ge sample into a Si(Li) detector, taken from Ref. 10. It was obtained by varying $\Delta\theta$ while holding $\varphi = 4$ mrad. Superimposed on the data points are curves of the relative x-ray fluorescence calculated for Ge atoms on the atomic planes (solid), and between the atomic planes (dashed) along the (220) reciprocal-lattice vector. The data are in moderate agreement with the theory, which takes into account the rapidly changing extinction depth in the vicinity of the diffraction condition, as well as the escape depth of the fluorescent radiation. Note that the calculated and

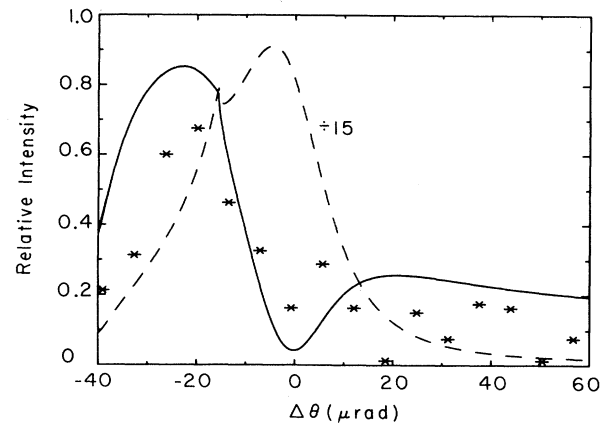


FIG. 10. Ge $L\alpha$ fluorescence measured (points) at the (220) diffraction condition at 8 keV while varying $\Delta\theta$ for $\varphi = 4$ mrad. For a uniform distribution of fluorescing atoms in the bulk of the crystal, the solid line gives the fluorescence calculated for atoms on the diffraction planes and the dashed line the fluorescence for atoms between the diffraction planes. The latter curve is more intense because absorption is lower for XSW between the diffracting planes and is scaled down accordingly.

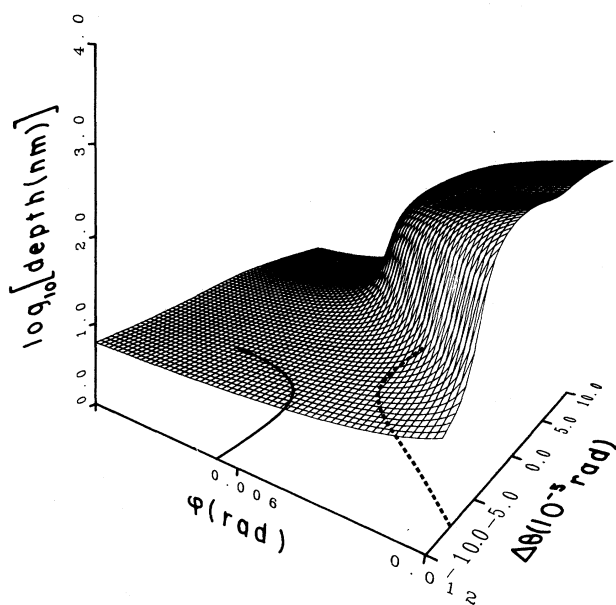


FIG. 11. Logarithm of the calculated penetration depth for the diffracted beam (β branch) for the Ge(220) reflection at 8 keV as a function of φ and $\Delta\theta$ (in rad). The positions of the α and β branches of the dispersion surfaces are plotted as described in Fig. 7.

measured fluorescence from the internal Ge atoms differs markedly from the fluorescence predicted from the field intensity seen by the atoms just at the surface (Fig. 10, $r=0$). Comparison of Fig. 10 with Figs. 8(a) and 8(c) shows that relatively strong fluorescent yields are obtained even when a reflected-diffracted beam is forbidden by (6), because the evanescent diffracted wave on the surface has a large amplitude.

The diffractive and standing-wave effects which have been observed for the interface of Ge with the vacuum apply equally well to the interface of a material with a lower susceptibility on top of a material with a higher susceptibility. GAXSW's parallel to the interface should

be observable even for an interface which is buried underneath the surface of a thin film, so long as the x-ray fluorescence or other indication of the atomic excitation is able to escape.

Furthermore, φ and θ can be chosen so that the wave penetrating the boundary is evanescent, thereby reducing background. Figure 11 shows the penetration depths calculated for the 8-keV (220) β -branch diffracted beam into the Ge crystal as a function of φ and $\Delta\theta$. At 8 keV it is possible to reduce the penetration depth into the Ge to 5 nm or less.

In summary, we have described an experiment which observes the fluxes of the specularly reflected and reflected-diffracted beams in the GAD geometry over the entire range of the diffraction process. The angular resolution and intensity of the incident beam obtained using a synchrotron-radiation source were sufficient to make direct comparisons to the two-beam dynamical theory calculated for diffraction from germanium at 8 keV. The observed intensities were normalized to the incident intensity, giving the first absolute measurements of this type. The observed intensities are in good agreement with the theory evaluated to first order, allowing for instrumental broadening, except for systematic deviations in the location of the β branch observed from reflection and diffraction for values of φ above the critical angle. It is proposed that the glancing-incidence diffraction geometry is a potentially useful one for the extension of the XSW method. It allows for the precise determination of atomic overlayer position parallel to the surface of a substrate and offers the possibility of making such a measurement on atoms at an interface which is deeply buried.

ACKNOWLEDGMENTS

The authors would like to thank Dr. A. Henins for assistance in preparing germanium crystal samples. Dr. W. Schildkamp and Mr. B. Blank made some highly appreciated improvements on our CHES monochromator. The experiment was conducted at CHES, which is supported by the U.S. National Science Foundation under Grant No. DMR-84-12465.

- ¹R. W. Wood, *Physical Optics*, 3rd ed. (McMillan, New York, 1934), p. 418.
- ²P. C. Clemmow, *The Plane Wave Spectrum Representation of Electromagnetic Fields* (Pergamon, Oxford, 1966).
- ³W. L. Marra, P. Eisenberger, and A. Y. Cho, *J. Appl. Phys.* **50**, 6927 (1979).
- ⁴A. M. Afanas'ev and M. K. Melkonyan, *Acta Crystallogr. Sect. A* **39**, 207 (1983).
- ⁵P. A. Aleksandrov, M. K. Melkonyan, and S. A. Stepanov, *Kristallografiya* **29**, 376 (1984) [*Sov. Phys.—Crystallogr.* **29**, 226 (1984)].
- ⁶A. V. Andreev, *Usp. Fiz. Nauk* **145**, 113 (1985) [*Sov. Phys.—Usp.* **28**, 70 (1985)].
- ⁷P. L. Cowan, *Phys. Rev. B* **32**, 5437 (1985).

- ⁸M. A. Andreeva and S. R. Borisova, *Kristallografiya* **30**, 849 (1985) [*Sov. Phys.—Crystallogr.* **30**, 493 (1985)].
- ⁹N. Bernhard, E. Burkel, G. Gompfer, H. Metzger, J. Peisl, H. Wagner, and G. Wallner, *Z. Phys. B* **69**, 303 (1987).
- ¹⁰P. L. Cowan, S. Brennan, T. Jach, M. J. Bedzyk, and G. Materlik, *Phys. Rev. Lett* **57**, 2399 (1986).
- ¹¹B. W. Batterman, *Phys. Rev.* **133**, A759 (1964).
- ¹²S. K. Anderson, J. A. Golovchenko, and G. Mair, *Phys. Rev. Lett.* **37**, 1141 (1976).
- ¹³P. L. Cowan, J. A. Golovchenko, and M. F. Robbins, *Phys. Rev. Lett.* **44**, 1680 (1980).
- ¹⁴B. W. Batterman and H. Cole, *Rev. Mod. Phys.* **36**, 681 (1964).
- ¹⁵A. L. Golovin and R. M. Imamov, *Kristallografiya* **29**, 410 (1984) [*Sov. Phys.—Crystallogr.* **29**, 248 (1984)].